ELSEVIER

Advances in Water Resources 24 (2001) 439–460

Advances in Water Resources

www.elsevier.com/locate/advwatres

A 2-D pore-network model of the drying of single-component liquids in porous media

A.G. Yiotis [a,b], A.K. Stubos [a], A.G. Boudouvis [b], Y.C. Yortsos [c,*]

[a] National Center for Scientific Research "Demokritos", Aghia Paraskevi 15310, Greece
[b] Department of Chemical Engineering, National Technical University of Athens, Zografos 15780, Greece
[c] Department of Chemical Engineering, University of Southern California, Los Angeles, CA 90089-1211, USA

Received 1 December 1999; received in revised form 30 May 2000; accepted 31 August 2000

Abstract

The drying of liquid-saturated porous media is typically approached using macroscopic continuum models involving phenomenological coefficients. Insight on these coefficients can be obtained by a more fundamental study at the pore- and pore-network levels. In this paper, we present a model based on a pore-network representation of porous media that accounts for various processes at the pore-scale. These include mass transfer by advection and diffusion in the gas phase, viscous flow in liquid and gas phases and capillary effects at the gas–liquid menisci in the pore throats. We consider isothermal drying in a rectilinear horizontal geometry, with no-flow conditions in all but one boundary, at which a purge gas is injected at a constant rate. The problem is mainly characterized by two dimensionless parameters, a diffusion-based capillary number, *Ca*, and a Peclet number, *Pe*, in addition to the various geometrical parameters of the pore network. Results on the evolution of the liquid saturation, the trapped liquid islands and the drying rate are obtained as a function of time and the dimensionless parameters. The importance of trapped liquid islands on screening mass transfer to the continuous liquid cluster is emphasized. For fixed parameter values, the drying front does not in general obey invasion percolation rules. However, as drying progresses, and depending on the relative magnitude of the capillary and Peclet numbers, a transition to a percolation-controlled problem occurs. Effects of capillarity and mass transfer on saturation profiles and drying rates are discussed. The results are then used to discuss upscaling to continuum models.

Keywords: Drying; Porous media; Pore network; Capillary pressure; Invasion percolation

1. Introduction

Drying of porous solids is a subject of significant scientific and technological interest in a number of industrial applications including coatings, food, paper, textile, wood, ceramics, building materials, granular materials, electronic devices and pharmaceuticals [1,4,7,19,20,27,28]. In a different context, drying in porous media is involved in distillation and vaporization processes associated with soil remediation [11], as well as in the recovery of volatile hydrocarbons from oil reservoirs by gas injection [15]. A variation of the latter is the main problem addressed here.

Generally, in drying, a single- or multi-component liquid phase gradually evaporates and is removed from the complex porous structure via combined heat and mass transfer processes. The traditional description relies on phenomenological approaches, in which the porous medium is a continuum, the dependent variables, like moisture content, are volume-averaged quantities and the relation of fluxes to gradients is through empirical coefficients [9,17,31–33]. Such approaches essentially ignore the effect of the pore microstructure which is of key importance for a quantitative understanding of the process. In fact, drying involves many pore-scale mechanisms, for example, the motion of individual gas–liquid menisci residing in the pore space, diffusion in the gas phase (for a single-component liquid) and the liquid phase (for a multi-component liquid), viscous flow in both phases, capillarity and possibly liquid flow through connected films, all of which need to be accounted for. We should note that although it also involves the receding of liquid–vapor interfaces, drying is not a typical external displacement process, like external drainage,

---

[*] Corresponding author. Tel.: 1-213-7400317; fax: 1-213-7408053.
E-mail addresses: giotis@chemeng.ntua.gr (A.G. Yiotis), yortsos@euclid.usc.edu (Y.C. Yortsos).

0309-1708/01/$ - see front matter © 2001 Elsevier Science Ltd. All rights reserved.
PII: S0309-1708(00)00066-X

Nomenclature

Roman letters

B	Bond number
C	concentration (kg/m^3)
C_e	equilibrium concentration (kg/m^3)
Ca	capillary number
D	diffusion coefficient (m^2/s)
F	evaporation rate (kg/s)
g	gravity acceleration (m/s^2)
k	permeability (m^2)
K_f	mass transfer coefficient along the fracture (m/s)
ℓ	distance between pore centers (m)
p	percolation probability of the invading phase
p_c	critical percolation probability of the invading phase
P	pressure (Pa)
Pe	Peclet number
q	percolation probability of the defending phase
q_c	critical percolation probability of the defending phase
Q	flow rate (m^3/s)
r	radius (m)
S	gas saturation
t	time (s)
t^*	time required for the liquid to evaporate at the maximum rate (s)
$u_{\ell n}$	liquid velocity (m/s)
u_{gn}	gas velocity (m/s)
u_n	velocity of the interface (m/s)
V_f	gas velocity through the fracture (m/s)

Greek letters

α	exponent of Eq. (5) that depends on the geometry of the fracture
γ	interfacial tension (N/m)
μ_g	viscosity of the gas phase (Pa s)
μ_ℓ	viscosity of the liquid phase (Pa s)
ρ_g	density of the gas phase (kg/m^3)
ρ_ℓ	density of the liquid phase (kg/m^3)
σ_{ft}	non-dimensionalised front width
Σ	variance of the pore-size distribution
X_{ft}	non-dimensionalised frontal position

which has been well studied in the past. Rather similarities exist to processes like solution gas drive and/or boiling in porous media, where the displacement of the liquid phase is driven internally by mass or heat transfer and which have been only relatively recently investigated [16,25].

The physical context of the problem considered here is schematically depicted in Fig. 1(a), which shows an exaggerated schematic of a fractured network. Liquid is trapped in the matrix and may vaporize as a result of an injected purge gas flowing primarily in the fractures. The actual overall problem is quite complex, requiring the consideration of the network of fractures and the matrix continuum, gas flow and mass transfer in the fracture network and the multi-dimensional mass transfer from the matrix continuum to the fracture network. For simplicity, we will consider the much simpler geometry of the pore-network model shown in Fig. 1(b), which involves a 2-D rectangular matrix block, all but one boundaries of which are impermeable to flow and mass transfer. We will also neglect gravity. Extension to 3-D geometries is, in principle, straightforward, although computationally costly, while equally feasible is the consideration of gravity effects. We consider isothermal conditions, under the assumption that heat transfer in the solid operates much faster than mass transfer in the gas phase. Finally, a single-component liquid phase is assumed. It is of note that this approach applies also to the vaporization of trapped NAPLs in low-permeability layers or regions [11].

At any time during the process, evaporation of the liquid leads to the receding of the liquid (drying) front, leaving behind disconnected clusters of liquid and liquid films (in corners of capillaries, or as thin films), the size and location of which change continuously with time. In general, four different spatial regions can be identified [30] (Fig. 1(c)):

(i) A far-field (from the fracture) region consisting of the initial liquid.
(ii) A region where both liquid and gas phases are macroscopically connected (this region may be absent in certain 2-D square pore networks for topological reasons).
(iii) A region where the liquid phase is disconnected and consists of individual clusters of variable sizes (trapped islands of liquid).
(iv) A near-field (to the fracture) region consisting primarily of the connected gas, with the liquid phase in the form of pendular rings, corner films or thin films on the solid surface, the thickness of which is progressively reduced towards a "totally dry" regime.

Evidently, the gas phase is macroscopically continuous in the last three regimes. On the basis of his experiments, Shaw [26] has postulated that liquid films may also provide hydraulic conductivity to the liquid phase in these regimes. We must point out that these four regimes only develop after the end of the Constant Rate Period (CRP). Prior to this, regions (iii) and (iv) cannot arise. Our model accounts for the full evolution of all these regimes, including the CRP, as will be shown below.

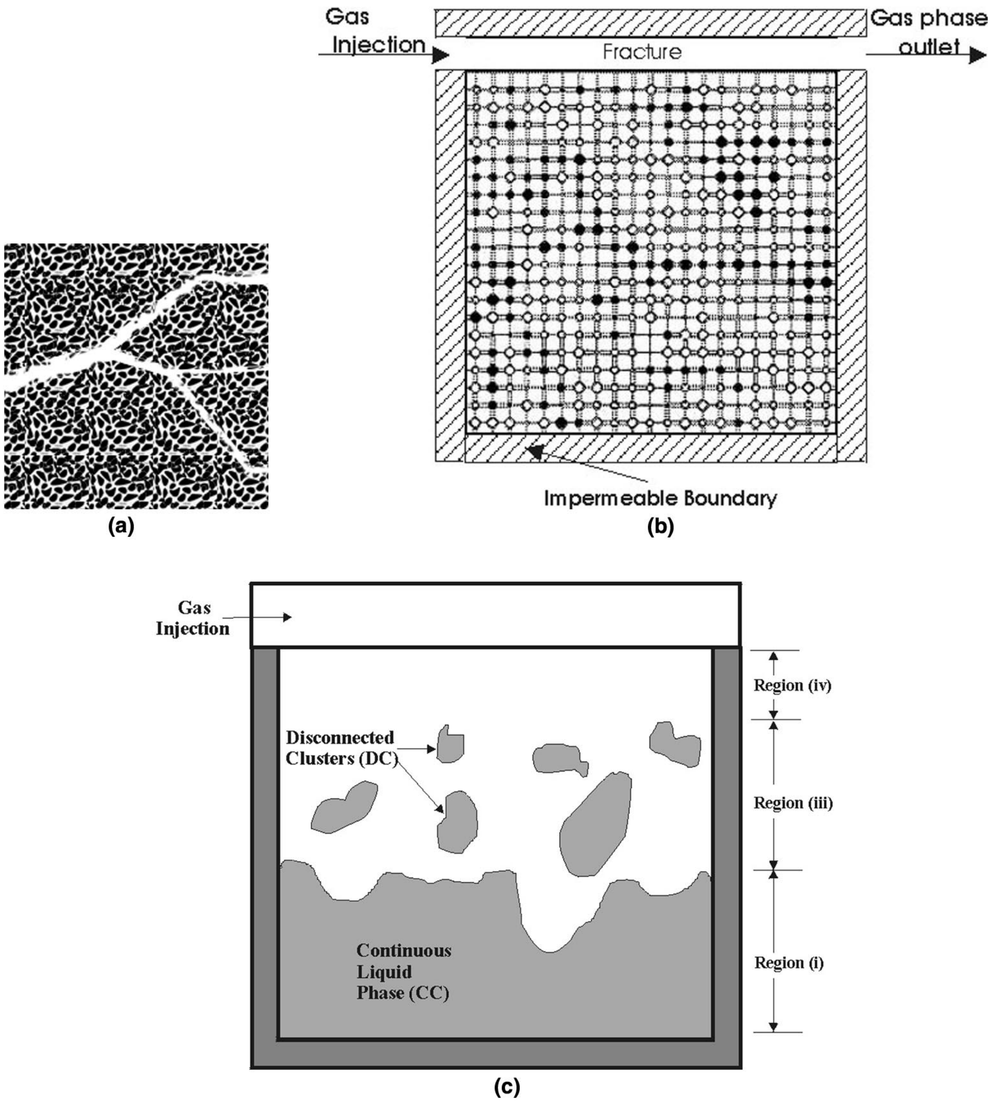

Fig. 1. (a) Schematic representation of fractured porous media. (b) Pore-network model representation of a porous medium. (c) Classification of typical saturation patterns.

The conventional approach to modeling drying is based on a continuum description, the simplest model for which involves only the two limiting regions (the far-field and the near-field), separated by a planar drying front. The latter recedes due to diffusion-controlled mass transfer obeying a square-root time dependence. More sophisticated continuum models have also been developed, as discussed by Luikov [17], and Whitaker [33], among others. Recently, Tsimpanogiannis et al. [30] proposed a more complex 1-D model using transverse-averages. Their model involves various coefficients, which need to be evaluated from a pore-network study, however (see also Stubos and Poulou [29]). Tsimpanogiannis et al. [30] also developed a theory based on pore-scale considerations, for the description of the scaling properties of the drying front. Specifically, they showed that consideration of viscous effects makes drying equivalent to Invasion Percolation in a Stabilizing Gradient (IPSG) (e.g., see Xu et al. [34]). In particular, they emphasized that liquid flow in the porous matrix is driven by capillary pressure gradients (the so-called capillary pumping or capillary wicking effect, [2]). The allowance of film flow could be an essential element of that theory. Based on the fact that drying is controlled by both capillarity and diffusion, in contrast to external drainage which is controlled by the injection rate, a power law relation of the evaporating front width with a modified, diffusion-based capillary number was obtained and shown to be compatible with the experimental data of Shaw [26]. However, other important features of the process, including the partition of the liquid phase in various regimes, the mass transfer rates, etc., were not explored.

Following recent trends in describing processes in porous media, several studies in recent years used a pore-network approach to model drying. Key to these approaches is the consideration of mass transfer, elements of which were described by Li and Yortsos [16] and Jia et al. [12], among others. Various pore-network models with specific applications to drying were proposed originally by Nowicki et al. [18], and more recently in a series of papers by Prat and co-workers [13,14,22,23]. In parallel, Pot et al. [21] used lattice-gas automata to simulate evaporation in a 2-D lattice. Nowicki et al. [18] presented a numerical simulation of the process at the pore-network level. However, the authors did not expand on the particular patterns and regimes obtained or on the associated effects on drying rates. Prat's studies represent the first attempt to characterize theoretically drying patterns and their rate of change in porous structures. Prat [22] studied the formation of drying patterns assuming capillary control, neglecting viscous effects and considering mass transfer only by quasi-static diffusion. Laurindo and Prat [14] provided a macroscopic assessment of the importance of liquid films. Based on percolation patterns and isothermal conditions, they computed drying rates by solving a quasi-static diffusion equation in the gas phase. Prat and Bouleux [23] focused on diffusional mass transfer and the effect of gravity on the front structure, but also commented on viscous effects. In earlier experiments using horizontal glass-bead packs [26], viscous forces were found to be important for explaining the formation of an evaporating front (separating continuous liquid from gas) of a finite size. More generally, we expect that advection and viscous effects will have an impact on patterns and drying rates. Existing pore-network models address mostly slow drying, controlled by capillarity and/or gravity and by diffusion, ignoring advection and/or viscous effects. We note that consideration of advection in the gas phase requires knowledge of the pressure field, which is coupled to viscous flow in the two phases and capillary effects. Thus, these two processes must be treated simultaneously.

The present paper is motivated by the above lack of completeness and attempts to shed light to mass transfer and/or viscous effects on the development of drying patterns. It is also motivated by the need to provide reliable coefficients in the appropriate continuum models, and in a sense it represents a continuation of the work by Tsimpanogiannis et al. [30], except that film flows are ignored. We consider the isothermal drying (at room temperature) of a porous block, initially saturated with liquid (hexane), subject to flow of air in the fracture and in the absence of gravity. The paper is organized as follows: First, we present details of the pore-network approach. The various mechanisms described previously (diffusion in gas phase, viscous flow in both phases, capillarity and capillary wicking) are addressed. Then, simulation results are obtained for the drying patterns and rates, for various values of the dimensionless parameters governing the process. The latter involve a mass transfer-based capillary number and the Peclet number based on the gas velocity in the fracture. The results are subsequently analyzed using simpler statistical theories, such as Invasion Percolation (IP). Various limiting cases are identified and analyzed. In particular, we pay attention to the trapped islands surrounding the drying front, which due to their screening effect on mass transfer play an important role in the problem. Scale-up issues as well as effects of various parameters not considered in the pore network are discussed in the last section.

2. Formulation

A discrete pore-network model is used to simulate the drying of a porous block. The porous medium is represented by the standard approximation of a 2-D network of spherical pore bodies connected through cylindrical pore throats [3,5] (Fig. 1(b)). The pore bodies serve as containers for either of the two phases and it is assumed that they have no capillary or flow resistance. Therefore, when a liquid–gas interface lies within a pore body, the pressures of both phases are taken to be equal and the interface recedes without any capillary forces restraining its movement (Fig. 2(b)). This simplification can be relaxed at the expense of higher computational cost and could be subject to the uncertainty of the precise pore body geometry. The throats serve as conductors of the flow and mass transfer and they act as capillary barriers. When a stationary liquid meniscus (interface) lies at the entrance of a throat adjacent to a liquid pore (Fig. 2(a)), an interfacial pressure difference, roughly equal to $2\gamma/r$, where γ is the surface tension and r the radius of the throat, develops between the two neighboring pores. The meniscus remains stationary until the pressure difference between the two pores exceeds that capillary pressure threshold. Then the meniscus will recede instantly (Figs. 2(c) and (d)), since it is assumed that the throat has no volume and the gas phase penetrates the pore. In our simulations, pore body and throat radii were uniformly distributed in the range 0.37–0.74 and 0.16–0.32 mm, respectively. The lattice length ℓ (pore center to pore center) was taken to be 2 mm.

The 2-D network has three sides impermeable to flow and mass transfer. Alternatively, one could impose periodic boundary conditions at the sides. Along the fourth side runs a fracture, which is represented as 1-D chain of pore bodies and throats. The two ends of the fracture are open to flow and mass transfer. Pore body and throat radii are taken equal to 0.77 mm and 0.275 mm, respectively. We note that the dimensions of the

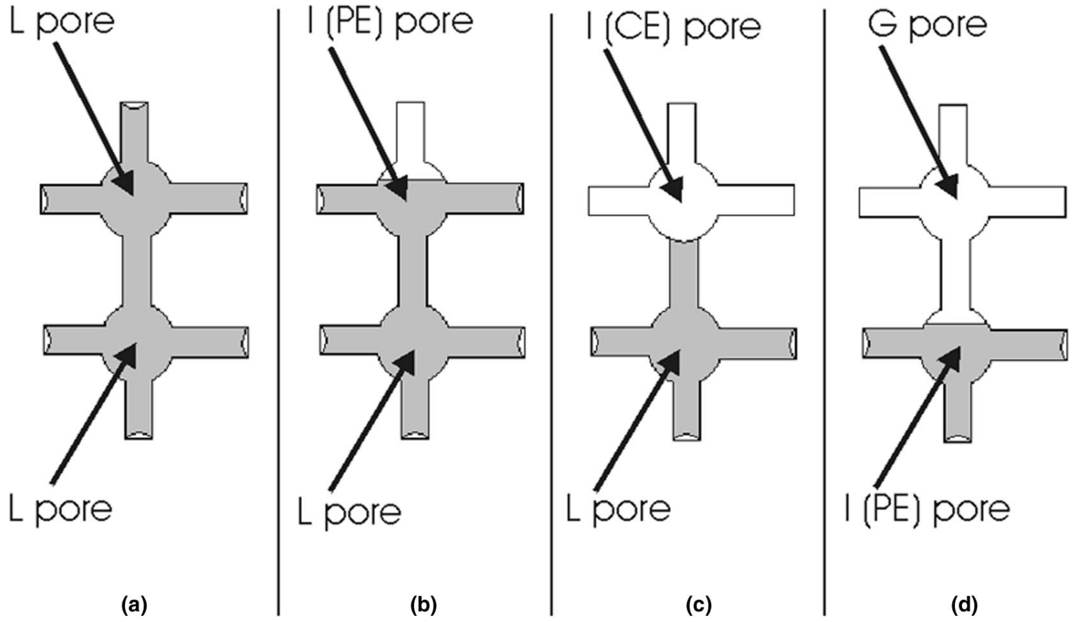

Fig. 2. The evolution of drying at an isolated DC consisting of two liquid pores. (a) Initially the cluster is surrounded by *I* pores of type CE. (b) When the pressure difference at the upper throat exceeds its capillary resistance, the meniscus recedes and the pore is penetrated by the gas phase. The same transition takes place between (c) and (d).

fracture considered in the simulations are comparable to the mean dimensions of the network. This is rather unrealistic, since one would expect that a real fracture would have larger dimensions than the network. However, it is adopted here, in order to emphasize viscous effects in the porous medium. Higher fracture dimensions would require unrealistically high gas flows for the pressure drop along the fracture to be sufficiently high to exceed the capillary pressure threshold at the throats of the network in direct contact with the fracture. The study of the viscous effects is one of the objectives of this work.

Initially the network is saturated by a single-component liquid (hexane). The fracture, however, contains only air at the beginning of the drying process. At one end of the fracture a purge gas (air) is injected at a constant volumetric rate. The concentration of the liquid component vapors is assumed to be zero at the entrance and the exit of the fracture at all times. Perhaps, a more appropriate Dankwerts type boundary condition, in which the concentration gradient is zero at the exit, could be used. The present condition exaggerates slightly the drying rate. The pressure is assumed equal to the atmospheric at the exit of the fracture and variable at the entrance of the flow, in order to maintain the constant rate condition. The gas injection results to a pressure gradient along the fracture, which eventually develops inside the porous block as well. As a result of the gas flow, the liquid evaporates initially at the interface pore throats along the fracture. Vapor flows by advection and diffusion.

Throughout the process, isothermal conditions are assumed, heat diffusion in the solid being faster than mass diffusion in the gas. This assumption will certainly not apply in the case of poorly conducting solids, however. The 2-D pore network is horizontal, thus gravity effects, which could be dominant, depending on the magnitude of the gravity Bond number [23], are not included. These can be readily implemented in the pore-network simulation. However, gravity can mask important mass transfer effects, while the understanding of the simpler drying process in its absence, is still incomplete, as noted above. Finally, the temperature is sufficiently far from the boiling point of the liquid, so that evaporation rates are diffusion-controlled and the binary mixture in the gas phase can be assumed to be dilute. Thus, the physical properties of the binary gas phase do not depend on the concentration of the liquid component vapors and are assumed to be constant and equal to those of the purge gas.

As a result of the ensuing drying process, the liquid will reside, in general, in two different and evolving regions (Fig. 1(c)): a "continuous" cluster (CC), which is part of the initial liquid cluster and can be defined as being "sample-spanning" across the two lateral edges of the matrix block; and various "disconnected" clusters (DC), which have become disconnected from the CC and from one another, and they are not "sample spanning" (see below). Their geometry, size, configuration and location are important to drying patterns and rates. Of course, initially, the porous medium is only occupied by a CC. It is the subsequent rate of change of CC and the formation of DC clusters, which is a main objective of this work. Liquid may also reside in films (thicker corner films or thin films) in gas-occupied pores, that may provide hydraulic continuity between clusters and/or with the fracture. These are not considered here, although in all likelihood, they have non-trivial effects on drying patterns and rates, as will be discussed below. Receding of the liquid–gas interface in the various clusters occurs when the capillary pressure across a meniscus first exceeds the capillary threshold at the pore where the meniscus resides. Accounting for capillarity requires the consideration of pressure fields in the liquid and gas phases. Flow in the latter is assumed to be slow and viscous-controlled. We will discuss this in more detail below.

In drying applications we can distinguish three types of pore bodies (Fig. 2): those fully occupied by gas (belonging to the gas phase and denoted by *G*), those fully occupied by liquid (belonging to the liquid phase and denoted by *L*) and those at the gas–liquid interface (in which a meniscus resides, denoted by *I*). The latter may be further subdivided in completely empty (CE) and partly empty (PE) pores [30]. As noted above, this classification does not account for corner films.

Liquid evaporates at the gas–liquid interface at rates determined by mass transfer in the gas phase, which are governed by advection and diffusion. The evaporation rate at *I*-type pores is equal to

$$F_{ij} = D\frac{C_i - C_j}{\ell}, \tag{1}$$

where F_{ij} is the evaporation flux through a throat connecting neighboring pores i and j, D is diffusion coefficient of the liquid component vapors in the gas phase through the porous medium, C_i is concentration at the liquid pore L, which is by default equal to the equilibrium concentration C_e of the liquid component vapors and C_j is the concentration at the I pore of type CE. Eq. (1) also applies to I pores of type PE, where the interface resides within the pore, the concentration in such pores also being equal to C_e, since they contain liquid. Then C_j is the concentration of the adjacent G pore (see Fig. 2(d)).

Mass transfer of the vapor in the gas phase obeys the convection-diffusion equation

$$\frac{\partial C}{\partial t} + \boldsymbol{u}\cdot\nabla C = D\nabla^2 C, \tag{2}$$

where C is the vapor concentration and $\boldsymbol{u}$ is the gas-phase velocity. In a G pore, this is further discretized as

$$V_i\frac{\Delta C_i}{\Delta t} = \sum_j\left[D\pi r_{ij}^2\frac{C_i - C_j}{\ell}\right] + \sum_j\left[\frac{\pi r_{ij}^4(P_i - P_j)}{8\mu_\mathrm{g}\ell}\overline{C}_{ij}\right], \tag{3}$$

where V_i is the volume of pore i, ΔC_i is change in C_i during the elapsed time Δt, r_{ij} is radius of the throat connecting pores i and j, μ_g is gas viscosity, P is pressure and C is the concentration at the pore. Note that the advection term is upstream weighted, namely

$$\overline{C}_{ij} = C_i \quad \text{if } P_i > P_j, \text{ and } \overline{C}_{ij} = C_j \text{ if } P_j > P_i.$$

In I pores of type CE the advection term of Eq. (2) is not accounted for

$$V_i\frac{\Delta C_i}{\Delta t} = \sum_j\left[D\pi r_{ij}^2\frac{C_i - C_j}{\ell}\right]. \tag{4}$$

The pressure fields are obtained from a separate computation to be discussed below. We note the use of a simplified Poiseuille-type approximation for the flow across two adjacent pores, and the assumption that mass transfer between the pores is by diffusion and convection (namely, dispersion in a single-pore is not considered). However, mass transfer between two adjacent pores, one of which resides in the fracture, is enhanced by considering a velocity-dependent mass transfer coefficient [24].

$$\left(\frac{K_\mathrm{f}\ell}{D}\right) = 1 + Pe^\alpha, \tag{5}$$

where the Peclet number, Pe, is defined as

$$Pe = \left(V_\mathrm{f}\frac{\ell}{D}\right), \tag{6}$$

α is an exponent that depends on the geometry of the fracture and V_f is the linear gas velocity through the fracture. Eq. (5) introduces a quasi-empirical macroscopic diffusion enhancement at the boundary between the matrix block (porous medium) and the free area of the fracture. This diffusion enhancement is an attempt to model the influence of the gas flow rate to the mass transfer enhancement along the convective layer within the fracture. When a neighboring pore contains a meniscus (PE), its concentration is the vapor equilibrium concentration. The boundary conditions for mass transfer involve zero flux at the lateral boundaries, a constant volumetric flux at the entrance of the fracture and zero concentration at the entrance and exit of the fracture. The latter could be modified to a zero-concentration gradient condition, but this was not considered.

The single-component liquid in the liquid phase and the non-condensable gas in the gas phase satisfy continuity equations. For their calculation, we solve for the pressure fields in G and L pores. Fluxes between adjacent pores of the same type are computed by Poiseuille-law type flow resistances, where the viscosity is taken constant

$$Q_{ij} = \left(\frac{P_i - P_j}{\ell}\right)\frac{\pi r_{ij}^4}{8\mu}, \tag{7}$$

$$\sum_j Q_{ij} = 0, \tag{8}$$

where μ is the viscosity of either of the two phases. The volumetric flux Q between an I of type CE pore and a L pore depends on the pressure difference between the two pores and the capillary pressure threshold of the connecting throat. We need to distinguish two cases: If the pressure difference between the two pores (capillary pressure) is not large enough for the gas phase contained at the I (CE) pore to penetrate the connecting throat, the meniscus remains stationary. However, as long as evaporation continues, there is a net liquid flow (but no non-condensable gas flux) in that direction. Then, in this pore we assign only a gas pressure value and zero mass flux rates of gas towards the L pore. In the next time step, the meniscus may be subject to a sufficiently high capillary pressure that can lead to the subsequent penetration of an adjacent pore and liquid displacement. Then, the meniscus recedes instantly and the L pore becomes of type I, PE. In I pores, a mass balance of the evaporating liquid gives the liquid velocity $u_{\ell n}$ at the interface as a function of the rate of emptying of the pore and the diffusive flux in the gas phase, namely [30]

$$-D\frac{\partial C}{\partial n} = \rho_\ell(u_{\ell n} - u_n), \tag{9}$$

where ρ_ℓ is the mass density of the liquid, u_n is normal velocity of the meniscus and n denotes the normal to the interface. Likewise, conservation of mass of the non-condensable gas leads to [30]

$$u_n = u_{gn}, \tag{10}$$

where u_{gn} is the gas velocity at the meniscus. These were used as interface conditions coupling the flow fields in the two phases. Therefore at liquid pores L adjacent to I pores of type CE, or at I pores of type PE adjacent to G pores, Eq. (7) has the following form which takes into account the above mentioned boundary conditions at the interface:

$$Q_{ij} = \left(\frac{P_i - P_j}{\ell}\right)\frac{\pi r_{ij}^4}{8\mu} + D\frac{C_i - C_j}{\ell\rho_\ell}\pi r_{ij}^2. \tag{11}$$

The first term on the right accounts for hydraulic flows towards (or from) adjacent L pores and the second term accounts for the evaporating volumetric flux towards the adjacent G pores or I pores of type CE. Taking into account the volumetric evaporation rate at all interface pores from Eq. (1) and the boundary conditions imposed to the interface by Eqs. (9) and (10) results to the well-known phenomenon of capillary pumping or wicking. This corresponds to a liquid viscous flow from I pores of type PE, where there is no capillary resistance to the receding of the interface, towards L pores adjacent to I pores of type CE, where the menisci remain stationary due capillary effects. The volumetric rate of flow is equal to evaporation flux so that the menisci remain stationary and the mass balance is satisfied. We note that the above treatment of mass transfer applies in the dilute limit. In the case of non-dilute mixtures, counter-diffusion in the gas phase needs to be considered as well. Finally, the gas saturation at I pores of type PE is calculated by the following mass balance

$$S_i^{t+1} = S_i^t + \frac{\Delta t}{V_i}\cdot\sum_j Q_{ij}, \tag{12}$$

where S_i^{t+1} is the gas saturation inside the pore at the next time step, S_i^t is the gas saturation at current time and Δt is the time step during which we assume constant flow rates Q.

For completeness, we provide a schematic of the way our algorithm accounts for the capillary pumping mechanism. As shown in Fig. 3, where two areas A and B along the interface are highlighted, if the throats R of the interface at area A have smaller radii than those of area B, they will result in higher capillary pressures Pc at the interfaces in area A. If the pressure in the gas phase is taken to be constant then we will have the logical sequence

$$R_A < R_B \rightarrow Pc_A > Pc_B \rightarrow P\mathrm{gas}_A - P\mathrm{liq}_A > P\mathrm{gas}_B - P\mathrm{liq}_B \rightarrow P\mathrm{liq}_B > P\mathrm{liq}_A$$

namely, due to the difference in radius, between the two sections of the interface, there results a capillary-induced liquid flow from area B to area A. In fact, during drying, the menisci in area A usually remain stationary and the evaporation flux from the interface of this section is balanced by the liquid flow towards section A from section B.

The simulation procedure in the network, the updating of interfaces and the marching in time is described in Appendix A and can be qualitatively summarized as follows. At any given time, sites have the designation, G, L or I, and pressure and concentration fields are known. The L sites can be part of the original liquid cluster (CC) or they belong to disconnected

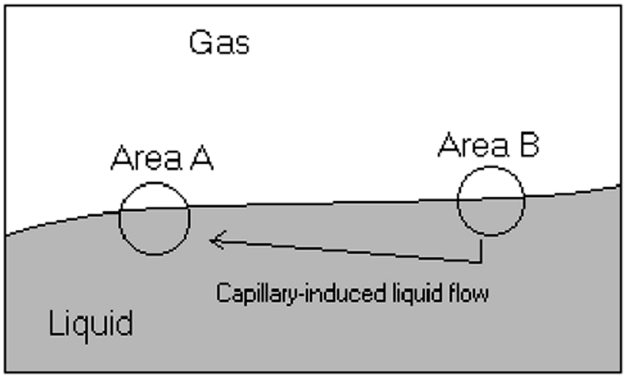

Fig. 3. Schematic representation of the capillary pumping phenomenon.

finite-size clusters (DC), which become trapped through the evaporation process. In the subsequent time step, the overall rate of evaporation from each of the liquid clusters is evaluated. Pressure fields are calculated and PE pores of type *I* are emptied according to the appropriate mass balances. The time step is selected such that it equals the minimum time required to empty completely any of the available PE pores. If at the current time, no PE pores are available to any (or all) of the clusters (namely all *I* pores are of the CE type) the throat with the smallest capillary threshold in the perimeter of any given cluster is the next throat to be invaded, at which time, the corresponding invaded pore becomes an *I* pore of the PE type. To determine this throat the liquid pressure is lowered uniformly in space inside the cluster, until the capillary pressure exceeds for the first time the smallest capillary threshold. Equivalently, this can be obtained by invading the throat with the smallest difference between the gas pressure in the pore and the corresponding capillary pressure threshold of the throat. Implicit to the above is the absence of hydraulic continuity between disconnected clusters, namely the absence of liquid films. Nonetheless, invasion must occur, since due to evaporation there is a continuous loss of mass from the liquid clusters. At the conclusion of the time step, concentration fields in the gas phase are computed and the process continues. This algorithm is essentially the same one used by Li and Yortsos [16] and Satik and Yortsos [25] in the related problems of phase change by solution gas-drive or boiling. All calculations are done explicitly in time. Pressure fields are computed using Successive Over-Relaxation, while concentration fields are obtained from (3) and (4) in a straightforward manner.

From a dimensional analysis of the problem, there are three main dimensionless groups: (i) a diffusion-based capillary number, *Ca,* defined as

$$Ca = D\mu_\ell C_e/\gamma\ell\rho_\ell, \tag{13}$$

where μ_ℓ is the viscosity of the liquid phase, expressing the ratio of viscous to capillary forces, based on a diffusion-driven velocity; (ii) a Peclet number, *Pe*, defined by (6), expressing the ratio of advection to diffusion in the gas phase, based on the linear velocity assuming only flow in the fracture; and (iii) the viscosity ratio, *M*, between liquid and gas viscosities. The latter is typically large and will not be considered in the sensitivity analysis to follow. We point out that one may also define a capillary number based on the fracture velocity. Clearly, the latter would control high-rate processes at early stages, while the diffusion-based capillary number controls the process at later times. These two capillary numbers are linearly related through the Peclet number, thus only two of these parameters are linearly independent. In the presence of gravity, an additional dimensionless number, the Bond number

$$B = \frac{g\left(\rho_\ell - \rho_g\right)k}{\gamma}, \tag{14}$$

expressing the ratio of gravity to viscous forces, must also be considered, where k is the permeability of the porous medium. Geometric parameters include the number of pores in the linear dimension $N = L/l$, where l is the typical pore length, the aspect ratio between mean pore size and pore length, as well as between mean pore size and mean throat size, a scaled variance of the size distribution, and the aspect ratio of the matrix block (here taken equal to 1). In this study, all geometric parameters are taken fixed, the aspect ratio of the matrix block is equal to 1, and emphasis is placed on the effect of the capillary and Peclet numbers. The effect of N will be addressed in the discussion on scale-up.

3. Results

A number of runs were conducted to simulate drying of liquid hexane in a matrix block of size 50 × 50. The corresponding physical parameter values are shown in Table 1. To carry out a sensitivity study, we varied the injection rate in the fracture, the interfacial tension and the diffusion coefficient. Table 2 shows the set of runs conducted. The characteristic time t^* denotes the time at which the matrix block empties at the maximum drying rate (which occurs at the first time step at which all liquid–gas interfaces are at the fracture-matrix boundary) and it is used to non-dimensionalise time. All simulations correspond to a fixed realization of the pore network, which allows studying the sensitivity of drying patterns and rates to the other parameters. Results on drying patterns, concentration profiles, transversely averaged saturation profiles and drying rates were obtained. We note that in order to demonstrate strong advection effects, the values of the Peclet number used in certain runs in the above table are high (perhaps unrealistically high).

We will use run 2 and run 15 to illustrate typical features from the simulation. These runs are typical of two limiting regimes, one in which capillary forces are dominant and mass transfer occurs by diffusion, and

Table 1
Values of physical properties used

Parameter	Value
Volumetric gas flow rates	$0.0 - 1.0 \times 10^{-6}$ m^3/s
Surface tension	19×10^{-3} N/m
Diffusion coefficient	6.38×10^{-6} m^2/s
Equilibrium concentration	0.266 kg/m^3
Liquid phase viscosity	2.85×10^{-4} Pa s
Gas phase viscosity	1.71×10^{-5} Pa s
Liquid phase density	650 kg/m^3
Gas phase density	4.4 kg/m^3

Table 2
Set of simulation runs

Run	Q (m^3/s)10^{-6}	γ (N/m)10^{-3}	D (m^2/s)10^{-6}	α	Ca	Pe	t^* (s)
1	1.00	19	6.38	0.33	1.68×10^{-6}	1325	14,238
2	0.45	19	6.38	0.33	1.68×10^{-6}	596	17,983
3	0.25	1.9	6.38	0.33	1.68×10^{-5}	331	21,340
4	0.25	19	6.38	0.33	1.68×10^{-6}	331	21,340
5	0.25	60	6.38	0.33	5.33×10^{-7}	331	21,340
6	0.25	100	6.38	0.33	3.20×10^{-7}	331	21,340
7	0.25	19	6.38	1.00	1.68×10^{-6}	331	500
8	0.25	19	63.8	0.33	1.68×10^{-5}	33	4002
9	0.20	19	6.38	0.33	1.68×10^{-6}	265	22,742
10	0.10	19	6.38	0.33	1.68×10^{-6}	132	27,645
11	0.05	1.9	6.38	0.33	1.68×10^{-5}	66	33,325
12	0.05	19	6.38	0.33	1.68×10^{-6}	66	33,325
13	0.015	19	6.38	0.33	1.68×10^{-6}	19	45,611
14	0.005	19	6.38	0.33	1.68×10^{-6}	6.7	57,819
15	0.0005	19	6.38	0.33	1.68×10^{-6}	0.66	88,752
16	0.0	19	6.38	0.33	1.68×10^{-6}	0.0	166,132

another in which viscous forces dominate and mass transfer is by advection. In addition, we will discuss a case (run 12) involving capillary control in the phase partition, but advection control in mass transfer. As schematically depicted in Fig. 1(c), the results show that the liquid phase consists of a main cluster (CC) and a

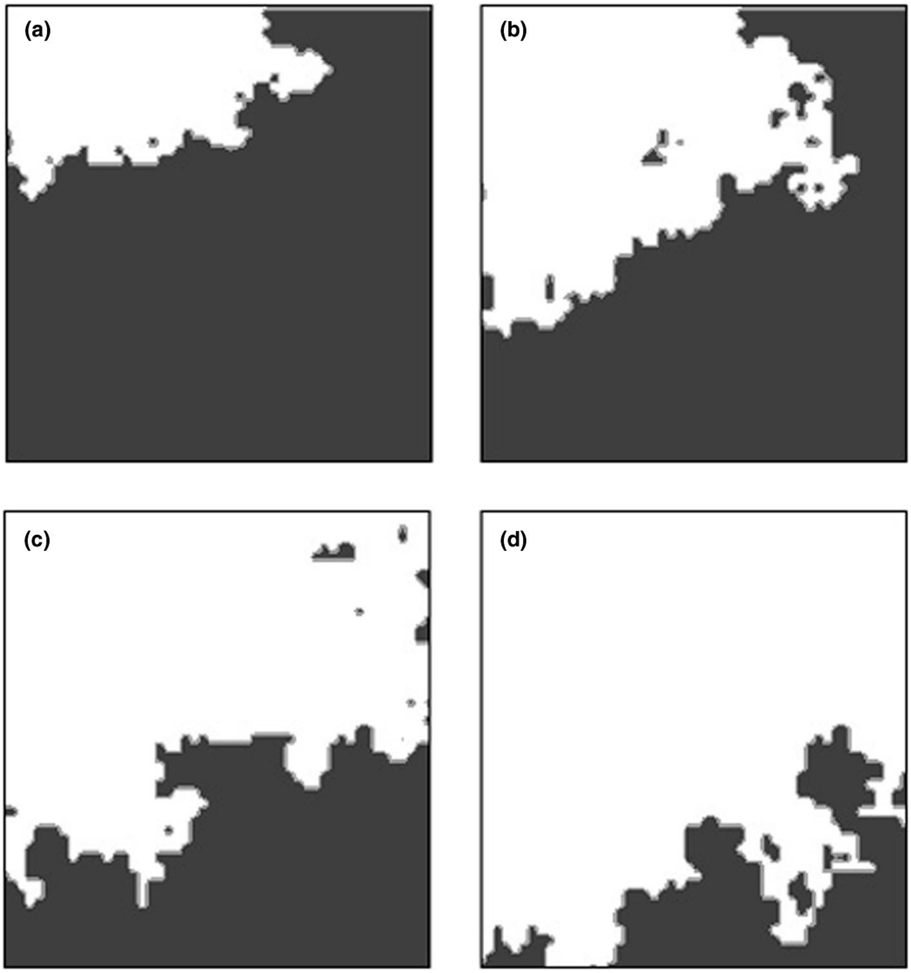

Fig. 4. Phase distribution patterns for run 2 ($Pe = 596, Q = 0.45 \times 10^{-6}$ m^3/s) at four different gas saturation fractions corresponding to 20%, 40%, 60% and 80% of the total pore volume. The liquid phase is black and the gas phase is white.

number of discontinuous (DC) clusters at the perimeter of the CC (see Figs. 4 and 5 for runs 2 and 15, respectively). These result from trapping of the liquid as the gas invades the liquid-occupied region. The patterns of the CC and/or the DCs depend on the value of the capillary pressure across the perimeter of each of these clusters as follows.

If viscous forces are not sufficiently strong across a given cluster (for example, as in run 15, Fig. 5), the capillary pressure variation is negligible, and the cluster takes the pattern of IP, in which the next throat to be invaded by the gas is that with the smallest capillary threshold (here, the one with the largest size) among all perimeter throats of that cluster. This condition depends on the value of the capillary number, the rates of drying (which also set viscous pressure gradients [30]) and the size of the cluster. Under otherwise similar conditions, small DCs are more likely to follow an IP pattern. A detailed check of the sequence of invasion showed that run 15 followed IP rules at any time during the process, while run 2 did not. Patterns corresponding to IP and diffusion-only mass transfer were obtained in run 16, where $Pe = 0$. The corresponding saturation patterns are shown in Fig. 6. Comparison with Figs. 4 and 5 shows substantial differences in the patterns between runs 2 and 15 (or 16) and some difference (at early times) between runs 15 and 16. The latter reflects mass transfer effects, due to the different Peclet numbers in the two runs.

Due to their relevance to real problems and the fact that capillary-dominated patterns eventually appear as late-time regimes, we provide here some additional discussion of their properties. We first recall that all simulations in this paper were conducted assuming the absence of film flows, thus DCs are hydraulically disconnected from each other and the CC. Under these conditions, in a capillary-controlled pattern (such as run 15 and 16), while each cluster obeys locally IP rules, the sequence of penetration is dictated by the mass transfer rates across the perimeter of each cluster. In the related study of Li and Yortsos [16] this process was termed

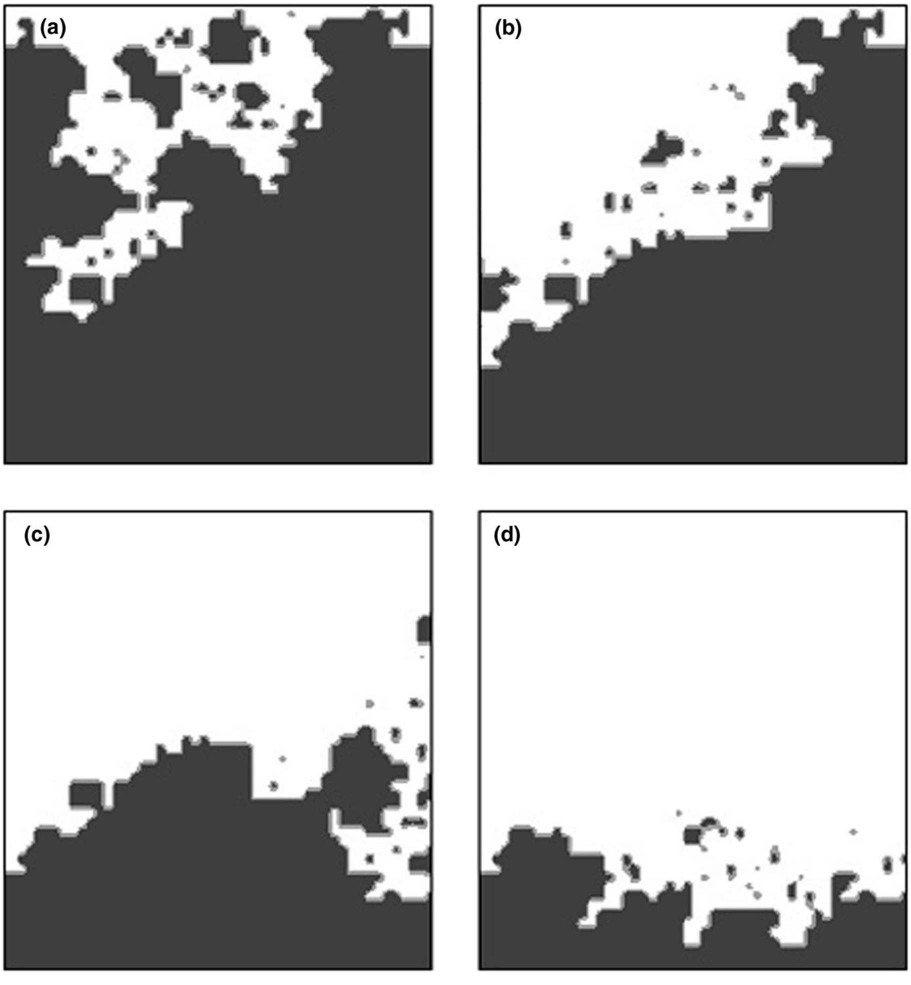

Fig. 5. Phase distribution patterns for run 15 ($Pe = 0.66, Q = 0.5 \times 10^{-9}$ m^3/s) at four different gas saturation fractions corresponding to 20%, 40%, 60% and 80% of the total pore volume. The liquid phase is black and the gas phase is white.

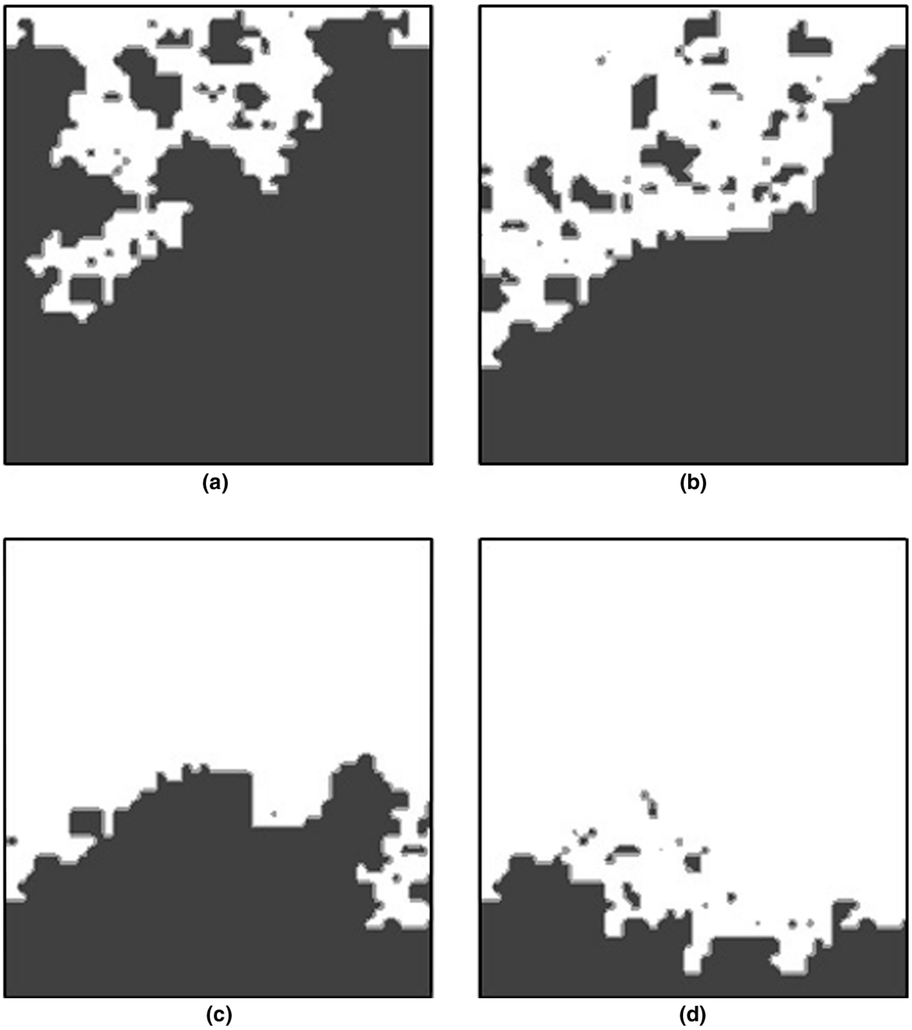

Fig. 6. Phase distribution patterns for run 16 ($Pe = 0, Q = 0.0$ m^3/s) at four different gas saturation fractions corresponding to 20%, 40%, 60% and 80% of the total pore volume. The liquid phase is black and the gas phase is white.

local percolation. Clusters closer to the open boundary are subject to a faster evaporation, compared to those further away, and are emptied faster. The end result is the development of gradients in the size of the isolated liquid clusters, with clusters closer to the fracture having smaller size (see also below). These gradients reflect mass transfer, rather than viscous effects. Nonetheless, the pattern of the CC is still dictated by IP rules. Clearly, however, the overall pattern would be a function of the drying rates, namely of the value of the *Pe*. We must note that under this regime of local percolation, different clusters may have different-size throats being invaded at the same time. In other words, it is possible that the drying of a given DC occurs by the emptying of a throat i, which is smaller than the largest perimeter throat, j, of another cluster, which due to negligible mass transfer is not being invaded (of course, as a result of capillary control, throat i is the largest among all perimeter throats of the first cluster).

The above analysis of capillary-controlled patterns is based on the assumption of negligible film flow. If, on the other hand, hydraulic continuity exists among all clusters (for example through liquid films) then, in the small *Ca* limit, the next throat to be penetrated will be the throat with the smallest threshold among *all* perimeter throats of *all* clusters. In the liquid-to-gas phase change study of Li and Yortsos [16], this was termed *global percolation.* In the absence of viscous or gravity gradients, such a process could lead to a deep penetrating front of a fractal nature, and liquid saturation gradients will not develop, in the sense that the proximity of a particular front site to the open boundary cannot influence the time at which it is invaded. Gradients in saturation will develop in the case of the viscous-capillary-gravity competition. This regime was implied in many previous studies, including the work of Tsimpanogiannis et al. [30]. We also note that deep penetrating fronts of fractal nature were not observed in

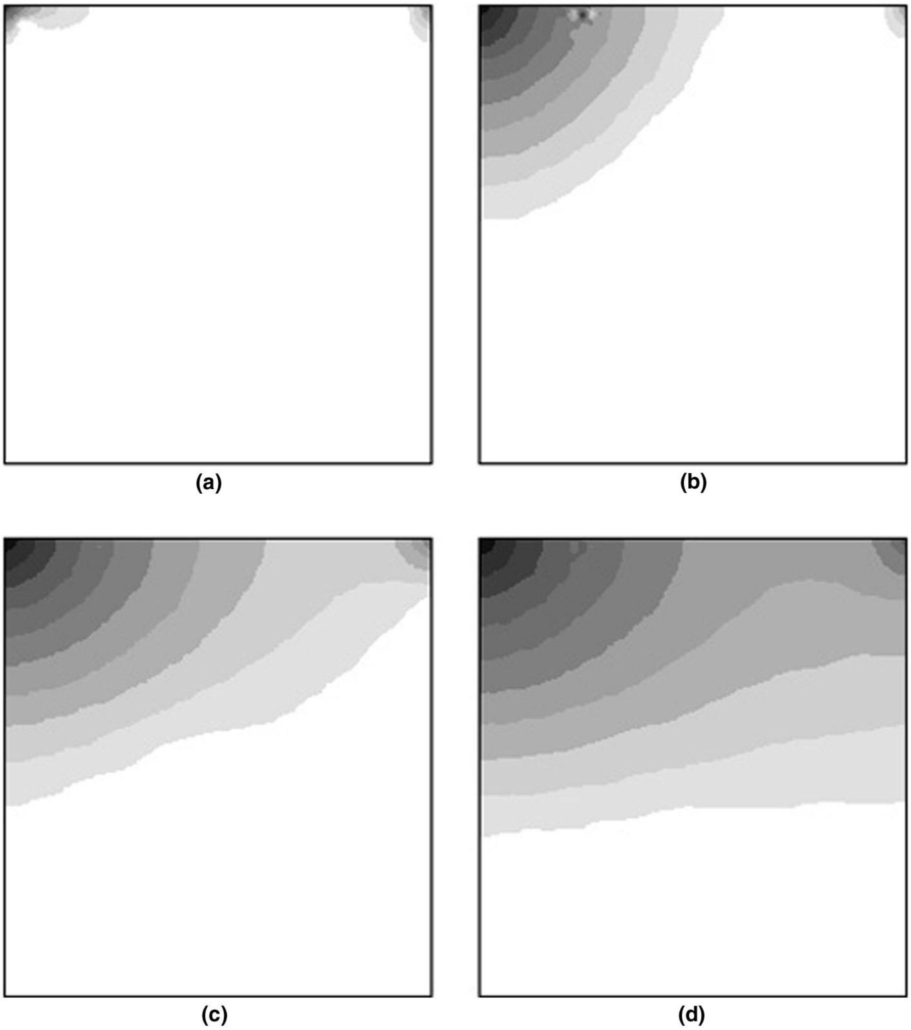

Fig. 7. Concentration patterns for run 15 ($Pe = 0.66, Q = 0.5 \times 10^{-9}$ m^3/s) at the four different occupation fractions. Darker colors indicate smaller concentrations.

the experiments of Ho and Udell [10]. Nonetheless, because of possible qualitative differences, it is evident that establishing hydraulic continuity is an important role played by liquid films and needs to be further explored.

In the limit when capillarity is negligible (as in run 2), the pattern deviates substantially from IP and almost follows a piston-like displacement (PD) (Fig. 4). Under these conditions, the capillary resistance of a throat is negligible, and the pattern is exclusively determined by mass transfer considerations, much like in the dissolution of a solid. The rate of generation of DCs and their size are smaller and the liquid phase consists mostly of a CC. Such conditions are not likely to persist for a long time in the typical case, however, where late-time drying patterns are likely to be of the IP type. We need to add that when viscous forces in the gas phase are important in setting the pattern (as is the case in run 2, for example), the receding of the CC has some of the properties of IPSG in a fracture-matrix system (Haghighi et al. [8]). In such cases, the higher capillary pressure upstream leads to a preferential invasion in the matrix in the upstream direction, thus leading to patterns that appear to be slanted (from the upstream to the downstream direction) as shown in run 2 (Fig. 4).

Regardless of the magnitude of the capillary forces, the presence of DCs is very significant in the development of the pattern. These clusters result in the screening of a part of the CC from the fracture, hence from the region of high concentration gradients, and lead to a balanced rate of drying between the two types of clusters, through the following stabilizing feedback mechanism. For example, if the mass transfer rates from the CC are too large, they will result in a faster rate of consumption of the CC, leading to the generation of a larger number of DCs, which in turn screen the CC from further mass transfer and slow down its rate of drying. Conversely, if the rate of drying of the CC is too small, most of the reduction in liquid saturation occurs from the DCs, the size and number of which decrease, leading to an increased mass transfer and a subsequent increased rate of consumption of the CC. It follows that for fixed values of the capillary and Peclet numbers, the statistics of the DCs, namely their number density and size distribution, remain approximately constant. In particular, the region where the DCs reside (which we may denote as the front region) is approximately of a constant width (Figs. 4–6). We should mention that similar findings were observed by Prat and Bouleux [23], although in the different situation where the gradients are provided by gravity rather than mass transfer. The size of the frontal region can be estimated using arguments from Invasion Percolation with Trapping (IPT) as described in Appendix B.

The screening of the CC from the region of high mass transfer is evident in the concentration profiles (Figs. 7 and 8). Depending on the value of the Peclet number and the location of the front, the concentration field in the gas phase may or may not be sensitive to the detailed structure near the front. For small values of the Peclet number (as in run 15, Fig. 7), the process is almost diffusion-controlled and the concentration resembles the much smoother concentration field surrounding an effective continuum (as also found by Li and Yortsos [16]). This despite the rather complex geometry of the front (see Fig. 5), which is rather complex (and in fact, fractal, e.g. see Feder [6]). Almost identical patterns were obtained for run 16 and they are not shown. As advection increases and at early times, however, the region of concentration gradients is a narrow boundary layer surrounding the front. At later times (panel 3 in Fig. 8), this is not uniformly developed, as poorly accessible regions cannot be effectively probed by the flow field. This mass transfer effect is also evident in the simulations of run 12 (Fig. 9). This run has a Peclet number almost two orders of magnitude larger than in run 15, although the sequence of the liquid patterns is

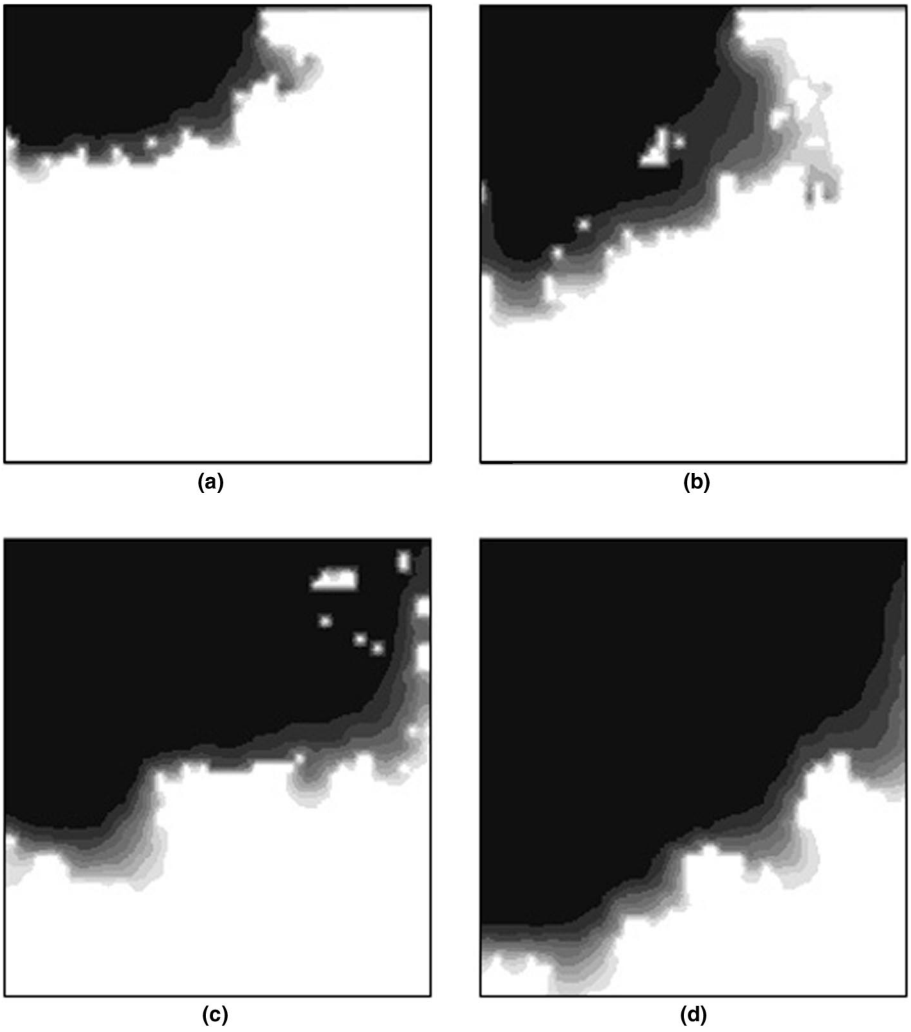

Fig. 8. Concentration patterns for run 2 ($Pe = 596, Q = 0.45 \times 10^{-6}$ m^3/s) at the four different occupation fractions. Darker colors indicate smaller concentrations.

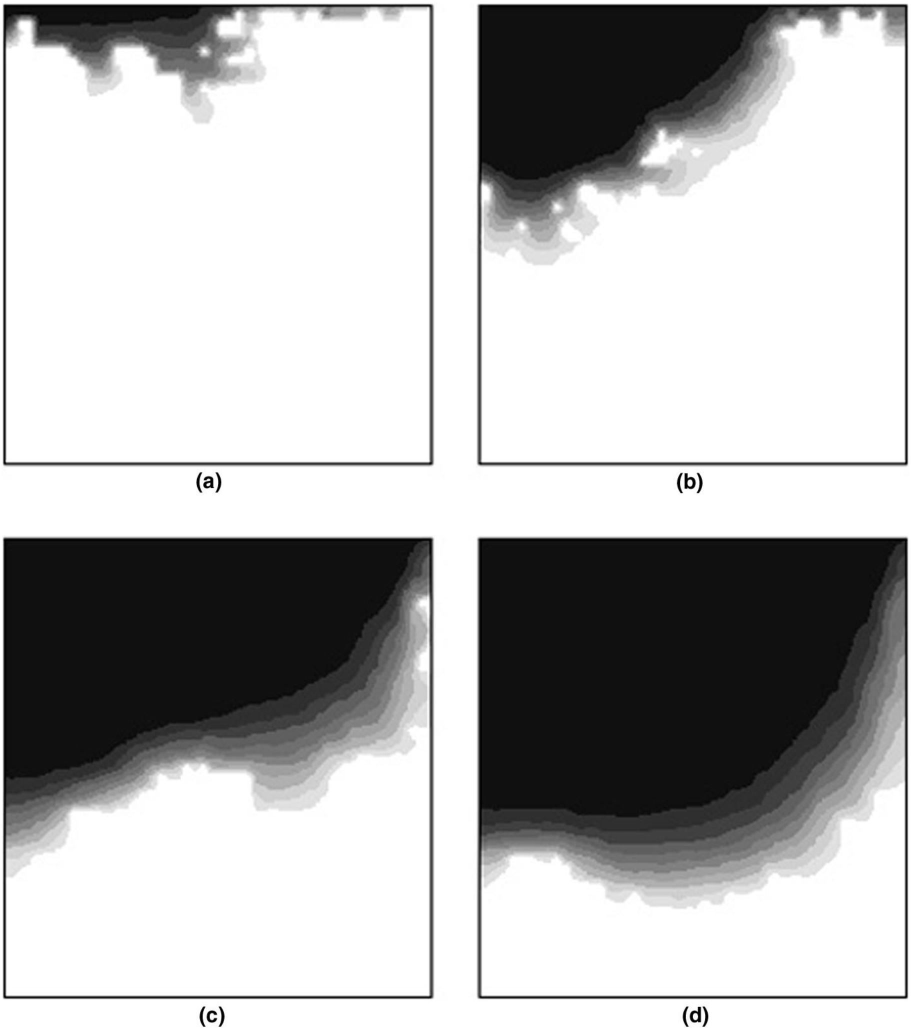

Fig. 9. Concentration patterns for run 12 ($Pe = 66, Q = 0.05 \times 10^{-6}$ m^3/s) at the four different occupation fractions. Darker colors indicate smaller concentrations.

almost identical (and is not shown here for simplicity). However, because of the much stronger advection effects, concentration profiles are much steeper in most places in run 12, resulting in proportionally higher drying rates (Fig. 9). At the same time, the effect is non-uniform spatially, and there exist regions in which diffusion is controlling. Strong advection effects similar to these were also reported in a related problem of bubble growth driven by heat transfer [25].

Runs 2 and 15 are typical of the two limiting regimes and can be analyzed in a relatively straightforward fashion. Intermediate patterns are more difficult to analyze, as they have features from both regimes. When both capillarity and viscous forces compete, the receding of the drying front does not follow strictly IP or PD rules. Depending on the rates of evaporation as well as the size of the individual clusters, there may exist more than one pore of the PE type at the same time, and these pores may not necessarily correspond to the IP or the PD sequence. We must point out that Tsimpanogiannis et al. [30] estimated the spatial extent over which the front follows IP rules using scaling arguments, from which the following relation was developed for 3-D patterns

$$\sigma_{\mathrm{ft}} \propto \left(\frac{2\Sigma X_{\mathrm{ft}}}{Ca} \right)^{0.47}, \tag{15}$$

where $\sigma_{\mathrm{ft}}, X_{\mathrm{ft}}, \Sigma$ are non-dimensionalised front width, frontal position and variance of the pore-size distribution, respectively. Implicit to this relation was the assumption of global percolation (namely of hydraulic continuity via film flow). This result is not expected to hold here. Nonetheless, clusters of small size will erode following local IP rules. In larger-size clusters, however, the spatial extent over which IP rules apply would be limited. Thus, the problem acquires some of the characteristics of IPSG [30]. As time increases, drying rates decrease, as the front recedes further away, and the width of the front, where IP is exhibited, increases

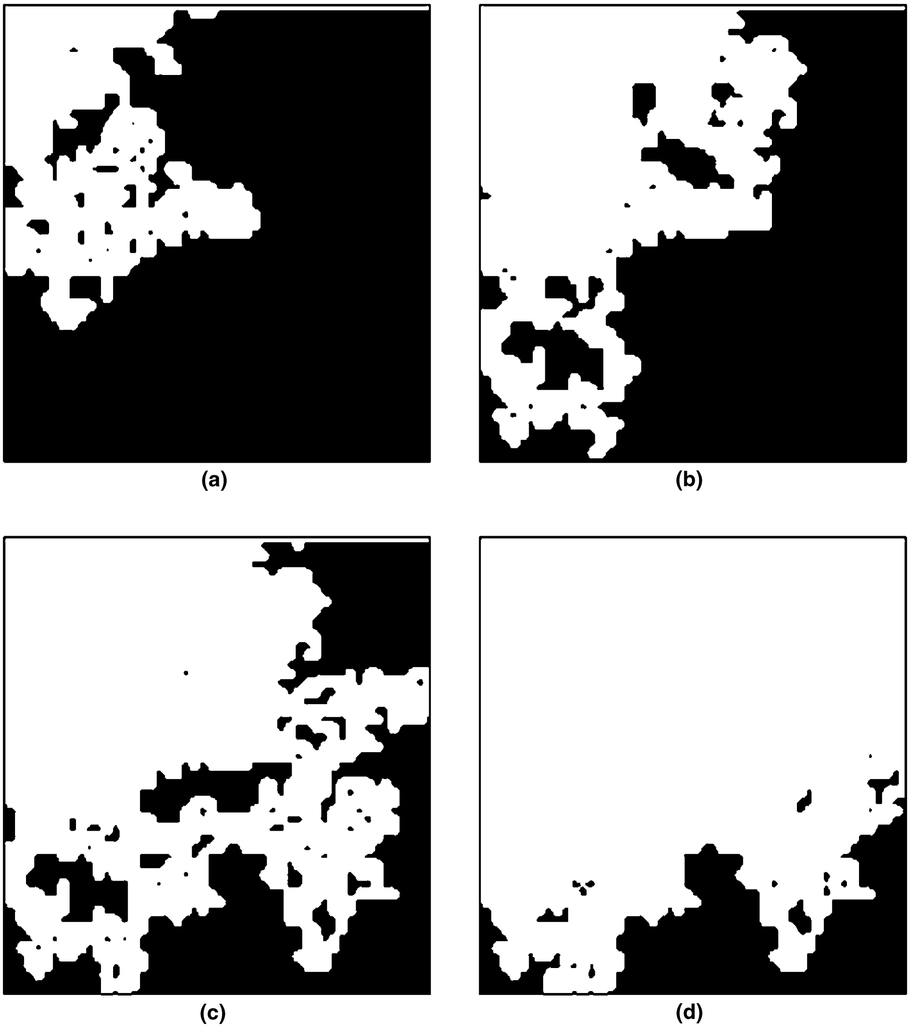

Fig. 10. Phase distribution patterns for run 4 ($Pe = 331, Q = 0.25 \times 10^{-6}$ m^3/s) at four different gas saturation fractions corresponding to 20%, 40%, 60% and 80% of the total pore volume. The liquid phase is black and the gas phase is white.

accordingly. One expects that after sufficiently long time, the process will approach a state where IP applies for all clusters. Some arguments from IPT are furnished in Appendix B to estimate the size of the front in this problem.

A typical case in which viscous and capillary forces compete is run 4, shown in Figs. 10 and 11. The invasion pattern belongs to neither of the two limiting regimes. There is evidence of IPSG in the matrix, similar to run 2, but also a multiple number of DCs, similar to run 15. The concentration profiles for this run (Fig. 11) are similar to those of run 12, and suggest substantial concentration gradients in boundary layer regions near the front. At the same time, regions far from the fracture are effectively being screened, despite the large Peclet number in this run, leading to mass transfer similar to the diffusion-controlled case (run 15).

In macroscopic continuum models a quantity of interest is the transverse-averaged saturation profiles. Results for runs 15, 12, 4 and 2 are shown in Figs. 12–15, respectively, for four different values of the fraction of the liquid volume occupying the matrix (and which corresponds to the four panels of the previous figures). As expected, runs 15 and 12 have almost identical profiles (Figs. 12 and 13), their patterns being dictated by IP rules, even though their mass transfer characteristics are not the same. Differences due to the latter are reflected in their drying rates to be discussed below. Gradients in saturation develop, due to the continuous receding of the front. As discussed above and in Appendix B, these gradients reflect the screening of inaccessible, deeper-lying parts of the liquid front from high concentration gradients, the resulting limited mass transfer, and the development of a frontal region of finite width (which is constant in the absence of viscous effects, but increases with time in their presence). The profiles in runs 4 and 2 (Figs. 14 and 15) reflect a more uniform penetration, at early times, due to the preferential receding of the liquid

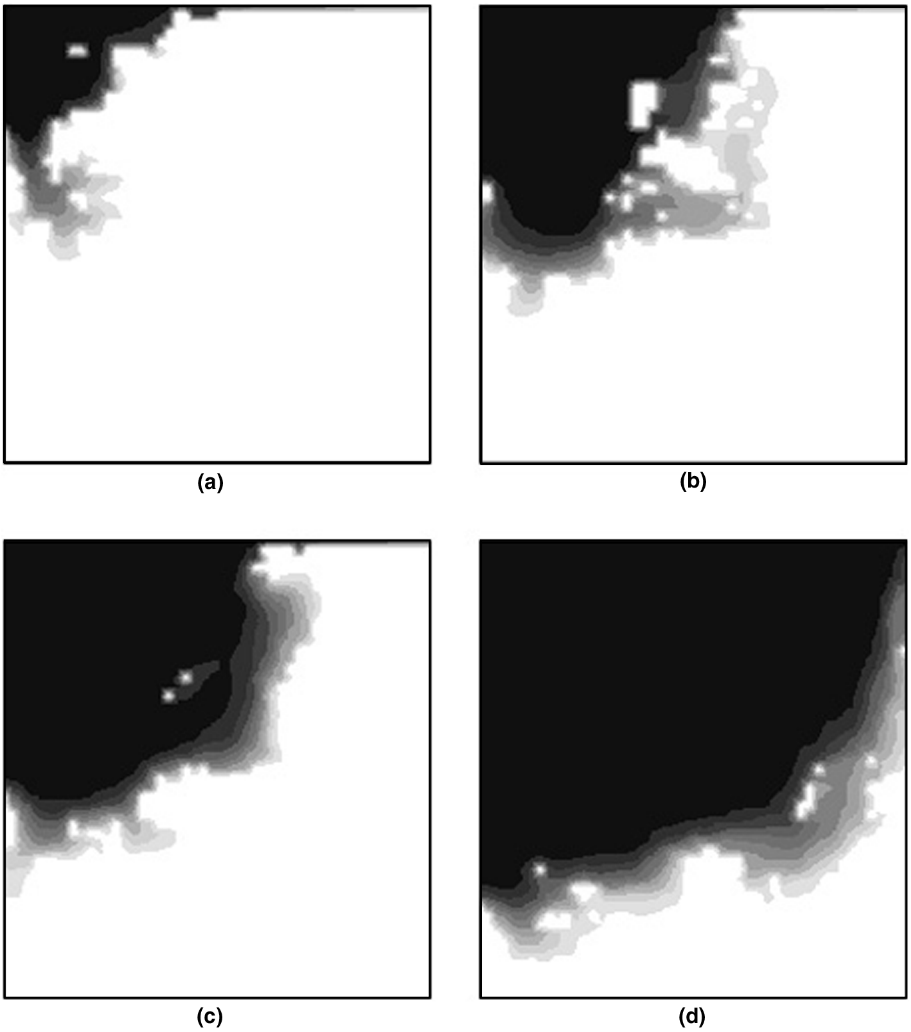

Fig. 11. Concentration patterns for run 4 ($Pe = 331, Q = 0.25 \times 10^{-6}$ m^3/s) at the four different occupation fractions. Darker colors indicate smaller concentrations.

in the upstream direction as a result of strong viscous effects. These are not unlike the profiles in the drainage of a matrix block [8]. As time increases, however, all profiles eventually approach a state which progressively becomes capillary- and diffusion-controlled.

Fig. 16 shows drying curves for the various runs simulated. As discussed, the time was made dimensionless with the time t^* it would take to empty the matrix block under conditions of the maximum rate. It then follows that the slope of the drying curves is the dimensionless rate of drying (relative to the maximum drying rate). Note that because the maximum rate depends on the Peclet number in the fracture (roughly as $Pe^{1/3}$) this plot emphasizes processes under convection control and should be interpreted with care, as far as the upscaling of the process is concerned. The figure shows clearly the existence of the conventional Constant Rate Period (CRP) (with the exception that film flow is not involved here) followed by a period of continuously declining rates. From an analysis of the patterns, we have found that the CRP lasts roughly until the time when the CC has lost continuity with the fracture. This is in qualitative agreement with indirect experimental findings from tests on chalk samples initially containing liquid pentane and dried by methane injection along the fracture [15]. In addition, macroscopic arguments set forth by Stubos and Poulou [29] on the basis of the same experimental data have led to the same conclusion. Indeed, as long as the liquid is continuously connected to the fracture, the combination of enhanced evaporation rate (through the coefficient given by Eq. (5)) and capillary gradients leads to a constant drying rate. This is evident when considering the low Peclet number run 15 or the IP run 16 in Fig. 16 where the CRP is very short due to the fast receding of the liquid phase from the fracture. A close examination of the drying curves shows that the highest rate and the longest CRP are found in run 4. In this “critical” case the gas pressure developing

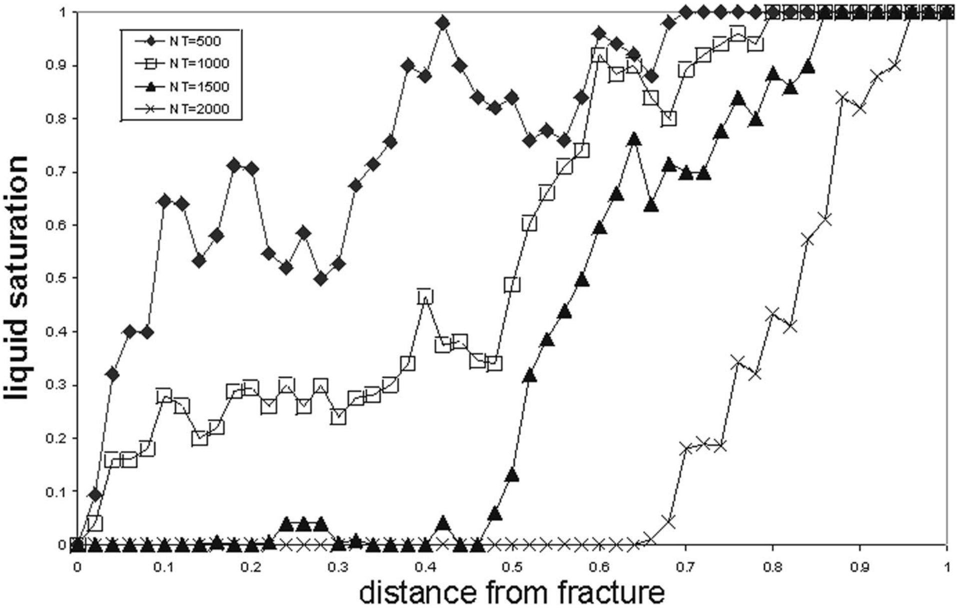

Fig. 12. Transversely averaged saturation profiles for run 15 at the four different occupation fractions.

close to the entrance of the fracture is high enough to cause the breaking of menisci in the left side of the matrix block. On the contrary, this cannot happen on the right side sustaining for relatively large times sufficient liquid contact with the fracture (see patterns in Fig. 10). Thus the constant rate during the CRP reflects the detailed mass transfer characteristics during the process and is realization-dependent. By increasing the interfacial tension value in run 4 (runs 5 and 6 of Table 2), we find that the drying rate and the CRP drop to levels similar to the ones determined for the low Peclet number cases (Fig. 17). In fact, the gas pressure is not any more sufficient to overcome the capillary thresholds and the case resembles more and more to IP. When γ decreases on the other hand (run 3), all menisci in contact with the fracture break at early times and the CRP is very short. The drying rate also drops accordingly (Fig. 17). For the case of IP-controlled processes, the end of the CRP in terms of the amount of liquid left can be readily estimated from the analysis in Appendix B.

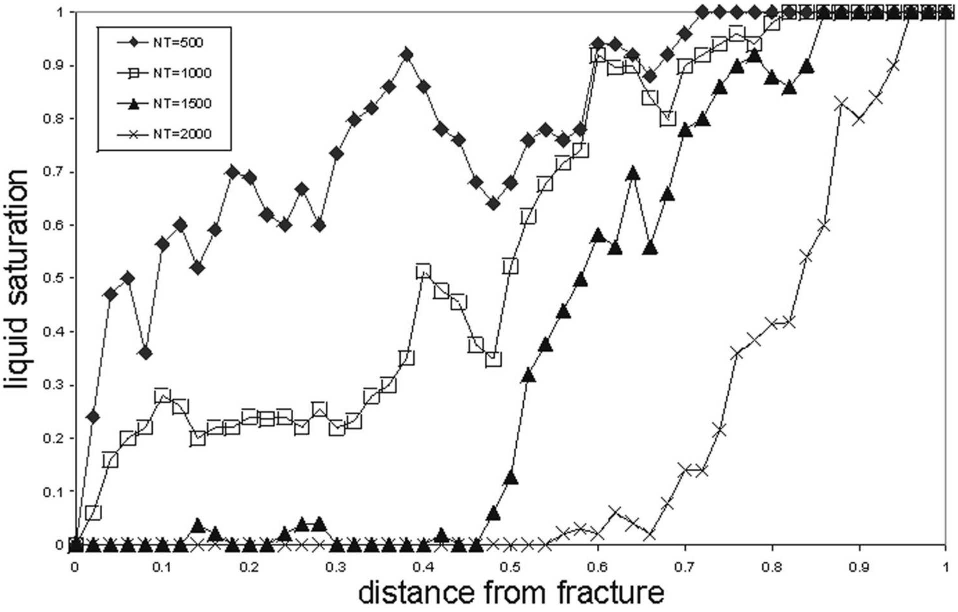

Fig. 13. Transversely averaged saturation profiles for run 12 at the four different occupation fractions.

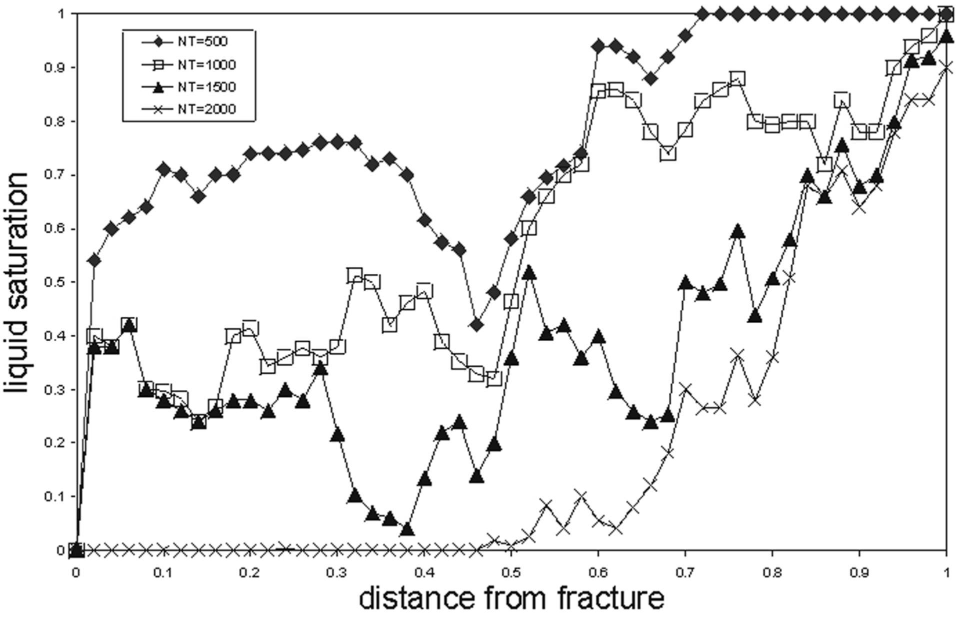

Fig. 14. Transversely averaged saturation profiles for run 4 at the four different occupation fractions.

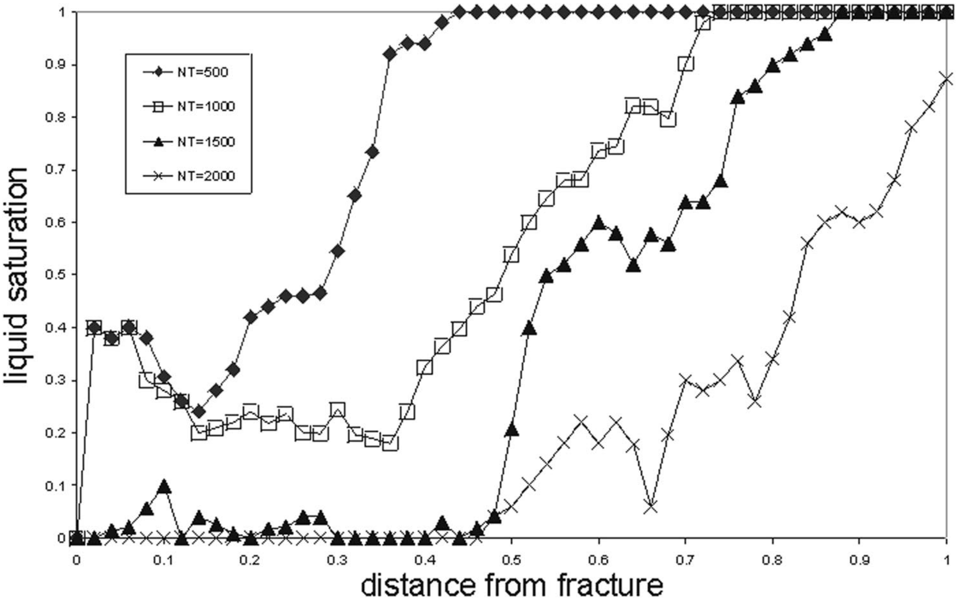

Fig. 15. Transversely averaged saturation profiles for run 2 at the four different occupation fractions.

4. Discussion

The above analysis was based on a number of simplifying assumptions, most of which were made to illustrate various effects. We single out the small size of the fracture pores and throats taken, in order to allow for a study of the viscous-capillary competition at the rates considered. At a larger contrast of fracture/matrix capillary and permeability characteristics, the onset of a PD regime will be delayed as far as the flow rate is concerned. We also note that the Peclet number in some of the runs can be considered unrealistically high. Such simulations were purposely made to exaggerate the effect of advection in mass transfer. In general, flow rate-driven effects will dominate the process at early times, and particularly during the CRP, which will be controlled, as a result, by the detailed geometry and process characteristics. It is in this regime and time period, where pore-network simulations, such as these, can have a significant impact. At later stages, the front recedes, viscous effects and advective mass transfer become less important and the process becomes capillary- and

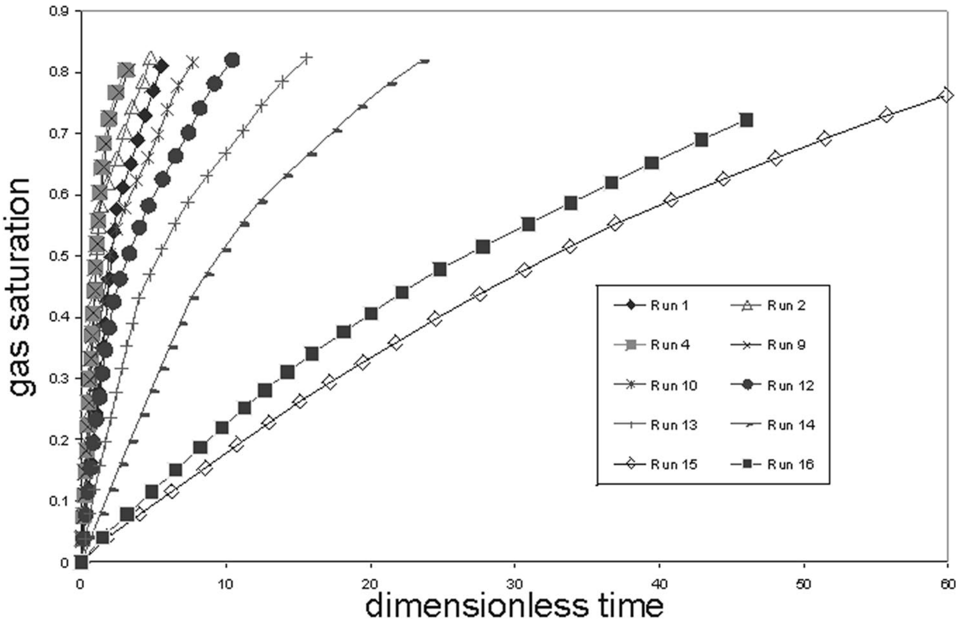

Fig. 16. Drying curves (gas volume fraction versus dimensionless time) for various runs.

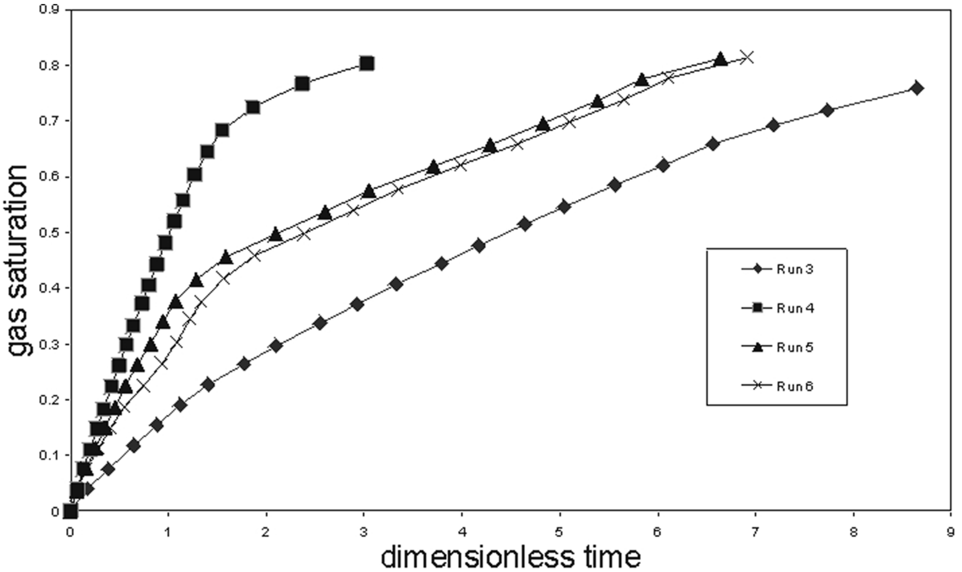

Fig. 17. Drying curves (gas volume fraction versus dimensionless time) for runs 3–6.

diffusion-controlled. In this regime, the analysis discussed in Appendix B applies and various results from the theory of IPT can be used to describe the process.

A key simplification made in the paper concerns the absence of liquid films. As discussed, these can be important in providing hydraulic continuity between clusters, which can drastically alter the patterns and the location and size of the DCs and the CC, and can possibly affect macroscopic capillary pressure–saturation relationships. Work in this direction, in particular in the incorporation of film flows in the pore-network simulation, is currently under way. At present, their effect is difficult to assess. We also need to mention the restriction to single-component liquids, which eventually leads to the complete evaporation of the liquid clusters. In the presence of a non-volatile component, the disconnected liquid clusters will not disappear, but will affect adversely the mass transfer rates. Such effects need to be considered as well.

The results can be used for upscaling to macroscopic continuum models. Following the CRP, where the process becomes capillary- and diffusion-controlled, the theory of IPT discussed in Appendix B can be used to elucidate the distribution of the liquid phase, and the size and extent of the DC region. This information can then be utilized to construct model diffusion problems, the solution of which can be implemented in the calculation of needed coefficients in macroscopic models (for example, as required in Tsimpanogiannis et al. [30]). Such work is also under way. On the other hand, the CRP is not necessarily amenable to such a statistical theory description, given that non-local effects of rate and viscous forces (or finite-size effects in the case of capillary control) are important. The solution of this problem must be sought by conducting extensive pore-network simulations, including the ensemble-averaging of results over many realizations, something that was not done here.

5. Conclusions

In this paper we presented a pore-network model for the drying of a single-component liquid in porous media. The model accounts for various processes at the pore-scale including mass transfer by advection and diffusion in the gas phase, viscous flow in liquid and gas phases and capillary effects at the gas–liquid menisci in the pore network. A 2-D version of the model under isothermal conditions in a rectilinear horizontal geometry was formulated. Drying is driven by the flow of a purge gas injected at a constant rate. The problem is characterized by two dimensionless parameters, a diffusion-based capillary number, *Ca*, and a Peclet number, *Pe*, in addition to the various geometrical parameters of the pore network. Results on the evolution of the liquid saturation, the trapped liquid islands and the drying rate were obtained as a function of time and the dimensionless parameters. In the absence of liquid film flow, the importance of trapped liquid islands in screening mass transfer to the continuous liquid cluster was emphasized. This results in saturation gradients, and the development of patterns which are different than in the case of flow continuity between the different clusters. For fixed parameter values, the drying front does not in general obey invasion percolation rules. However, as drying progresses, and depending on the relative magnitude of the capillary and Peclet numbers, a transition to a percolation-controlled problem occurs. In fact, it is likely that such is the case in many realistic situations. Effects of capillarity and mass transfer on saturation profiles and drying rates were discussed. The results provide insight on the process. The pore-network simulation can also be used to provide expressions for various coefficients in macroscopic continuum models, currently treated empirically. Work in this direction is in progress.

Acknowledgements

The research of one of the authors (YCY) was partly supported by DOE contract DE-AC2699BC15211, the contribution of which is gratefully acknowledged. Partial funding by the JOULE Program of the European Commission is also acknowledged (Contract JOF3-CT95-0008). We acknowledge useful discussions with S. Poulou and I.N. Tsimpanogiannis.

Appendix A

The essential elements of the algorithm are described below:

1. A random network of pores and throats is created using a uniform size distribution between the specified values.
2. The pressure drop along the fracture is calculated using Eqs. (7) and (8).
3. All liquid–gas interfaces of isolated liquid clusters (DCs and the CC) are located and the type (*I*-CE or *I*-PE) of their interface pores is identified.
4. Flow conductivities at all network throats are calculated. When a liquid meniscus within a throat is found to be stationary then a zero hydraulic conductivity is assigned to the gas phase adjacent to it.
5. All throats where gas penetration occurs as the local capillary pressure exceeds the capillary pressure threshold are identified. If there is no such throat at a specific cluster, then the gas penetrates the throat that has the lowest capillary threshold along the interface, i.e., the one with the largest radius.
6. The evaporation rate through every throat across all interfaces is calculated using Eq. (1).
7. The pressure fields in both liquid and gas phases are solved, using Eqs. (7), (8) and (11).
8. The *I* pore of type PE that will be emptied first at the current flow rates is located and the corresponding time required is identified. These pores loose mass due to both evaporation and the viscous flows of the capillary-pumping phenomenon (as shown by Eq. (11)).
9. The time step is selected taking care not to allow the concentration value at a gas pore to drop below zero or exceed the equilibrium concentration.
10. The concentration field is calculated in the gas phase using Eqs. (3) and (4) for the current time step. This calculation is straightforward based on the values of concentration at the end of the previous time step.
11. The gas saturation is calculated through Eq. (12) at all *I* pores of type PE for the current flow rates using the current time step.
12. If at the end of the current time step a pore becomes fully filled with gas (*I* pore of type CE) at any of the liquid clusters, the algorithm returns to step 3. If,

despite the fact that gas saturation at all penetrated interface pores increases, there is no pore completely filled with gas at the current time step, then the return is to step 6.

The above procedure is repeated until all liquid in the porous media has evaporated.

Appendix B

DCs form as the perimeter of the CC recedes, due to gas invasion, and the receding phase becomes trapped. In the absence of mass transfer considerations and under capillary control, this is the well-known mechanism of IPT. In the latter, the statistics of the trapped clusters can be determined from knowledge of the percolation probability, q, at which the defending phase (here the liquid) is being invaded. In the particular process under consideration, the invasion of the CC is a drainage process in which the invading (gas) phase percolation probability is near its percolation threshold

$$p \sim p_c (= 1/2 \quad \text{for a 2-D square lattice}).$$

Then, the defending phase is at percolation probability $q = 1 - p \sim 1 - p_c$. Knowledge of q allows one to estimate various statistics of the disconnected, trapped clusters, since the latter can be accurately approximated by the finite-size clusters of a mixed site-bond percolation process at percolation probability q. For example, the size of the largest DC follows the percolation scaling

$$\xi \sim \mid q - (1 - p_c) \mid^{-\nu},$$

where ν is the correlation length exponent. Statistics are also available (or can be obtained) for other properties of these finite-size clusters. In the above, it is implicitly assumed that $p_c < 1/2$, and that $\xi \ll N$. When the latter condition fails, as is the case in the simulations here, where $p_c = 1/2$, the largest (cut-off) size is set by the width of the lattice N. The above analysis can be used to estimate the statistics of screened DCs around the front, which are not subject to substantial drying rates, although not of the DCs at the frontier with the gas phase, which are being exposed to strong concentration gradients and a time-varying size.

In the presence of viscous effects, the invasion process is similar to IPSG, in which, in the absence of mass transfer effects, the largest size of the DCs is set by the Bond number of the process, namely

$$\xi \sim B^{-\nu/(\nu+1)}.$$

In drying, an equivalent Bond number can be defined as follows [30]

$$B = \frac{Ca}{2\Sigma X_{\mathrm{ft}}}.$$

However, the incorporation of an IPSG theory in the trapping problem is yet to be done. In general, we expect that such a theory would lead to the result that the average size of the DCs becomes smaller as viscous forces increase, as is the case with the problem without trapping [30], and also as shown in the simulations.

We also conjecture that the same length scale, namely the average size of the largest DC, is also the scale for the width of the frontal region, namely the region containing the trapped clusters (DC). Indeed, as we argued in the main text, the mass transfer screening from the DCs sets the balance between them and the CC. We expect that at least for diffusion-controlled problems, this screening will be effectively set by the distance between DCs, which are all sources of constant concentration. Given that the only characteristic length in the problem is the average size of the DCs completes the argument in support of this conjecture.

References

[1] Bruin S, Luyben KCAM. Drying of food materials: a review of recent developments. Adv Drying 1980;1:155–215.

[2] Ceaglske NH, Hougen OA. Drying granular solids. Ind Eng Chem 1937;29:805–13.

[3] Chandler R, Koplik J, Lerman K, Willensen JF. Capillary displacement and percolation in porous media. J Fluid Mech 1982;119:249–67.

[4] Chen P, Pei DCT. A mathematical model of drying processes. Int J Heat Mass Transfer 1989;32:297–310.

[5] Fatt I. The network model of porous media. Trans AIME 1956;207:144–81.

[6] Feder J. Fractals. New York: Plenum; 1988.

[7] Fortes M, Okos MR. Drying theories: their bases and limitations as applied to food and grains. Adv Drying 1980;1:119–54.

[8] Haghigi M, Xu B, Yortsos YC. Visualization and simulation of immiscible displacement in fractured systems using micromodels: I. Drainage. J Coll Interf Sci 1994;166:168–79.

[9] Hartley JG. Coupled heat and moisture transfer in soil: a review. Adv Drying 1987;4:199–248.

[10] Ho CK, Udell KS. An experimental investigation of air venting of volatile liquid hydrocarbon mixtures from homogeneous and heterogeneous porous media. J Contam Hydrol 1992;11:1–26.

[11] Ho CK, Udell KS. Mass transfer limited drying of porous media containing an immobile binary liquid mixture. Int J Heat Mass Transfer 1995;38:339–50.

[12] Jia C, Shing K, Yortsos YC. Visualization and simulation of non-aqueous phase liquids solubilization in pore networks. J Contam Hydrol 1999;35:363–87.

[13] Laurindo JB, Prat M. Numerical and experimental network study of evaporation in capillary porous media. Phase distributions. Chem Eng Sci 1996;51:5171–85.

[14] Laurindo JB, Prat M. Numerical and experimental network study of evaporation in capillary porous media. Drying rates. Chem Eng Sci 1998;53:2257–69.

[15] Le Gallo Y, Le Romancer JF, Bourbiaux B, Fernades G. SPE paper 1997;38924.

[16] Li X, Yortsos YC. Theory of multiple bubble growth in porous media by solute diffusion. Chem Eng Sci 1995;50:1247–71.

[17] Luikov AV. Heat and mass transfer in capillary-porous bodies. Oxford: Pergamon Press; 1966.

[18] Nowicki SC, Davis HT, Scriven LE. Microscopic determination of transport parameters in drying porous media. Drying Tech 1992;10:925–46.

[19] Pan SX, Davis HT, Scriven LE. Modeling moisture distribution and binder migration in drying paper coatings. Tappi J 1995;78:127.

[20] Panagiotou NM, Stubos AK, Bamopoulos G, Maroulis ZB. Drying kinetics of a multi-component mixture of organic solvents. Drying Tech 1999;17:2107–22.

[21] Pot V, Appert C, Melayah A, Rothman DH, Zaleski S. Interacting lattice gas automaton study of liquid–gas properties in porous media. J Phys II 1996;6:1517–34.

[22] Prat M. Isothermal drying of non-hygroscopic capillary-porous materials as an invasion percolation process. Int J Multiphase Flow 1995;21:875–92.

[23] Prat M, Bouleux F. Drying of capillary porous media with a stabilized front in two dimensions. Phys Rev E 1999;60:5647–56.

[24] Quintard M, Whitaker S. Convection, dispersion, and interfacial transport of contaminants: homogeneous porous media. Adv Water Res 1994;17:221–39.

[25] Satik C, Yortsos YC. A pore network study of bubble growth in porous media driven by heat transfer. J Heat Transfer 1995;118:455–62.

[26] Shaw TM. Drying as an immiscible displacement process with fluid counterflow. Phys Rev Lett 1987;59:1671–4.

[27] Simpson WT. Drying wood: a review. Drying Tech 1983;2:235–64.

[28] Simpson WT. Drying wood: a review. Drying Tech 1984;3:353–68.

[29] Stubos AK, Poulou S. Oil recovery potential from fractured reservoirs by mass transfer processes. SPE paper 1999;56415.

[30] Tsimpanogiannis IN, Yortsos YC, Poulou S, Kanellopoulos N, Stubos AK. Scaling theory of drying porous media. Phys Rev E 1999;59:4353–65.

[31] Van Brakel J. Mass transfer in convective drying. Adv Drying 1980;1:212–67.

[32] Waananen KM, Litchfield JB, Okos MR. Classification of drying models for porous solids. Drying Tech 1993;11:1–40.

[33] Whitaker S. Heat and mass transfer in granular porous media. Adv Drying 1980;1:23–61.

[34] Xu B, Yortsos YC, Salin D. Invasion percolation with viscous forces. Phys Rev E 1998;57:739–51.